Towards Certification-Ready Designs: A Research Investigation of Digital Twins for High-Performance Engineering

J. W. Quan, T. Fogel
(Autodesk Research, Toronto, Canada);
Z. Tenaglia
(Autodesk Research, Boston, United States);
A. Barker
(Autodesk Research, Birmingham, United Kingdom);
Z. J. Zhang
(Autodesk Research, Toronto, Canada);

Abstract

As aerospace and automotive industries increasingly adopt advanced materials and manufacturing methods, traditional certification processes, which rely on safety factors, historical data, and physical testing, struggle to address the complex failure modes of new materials like custom composites and additively manufactured structures. Digital twins—virtual replicas of physical systems—can enhance certification workflows by enabling continuous monitoring and providing real-time insights into system performance through the integration of sensor data with physics-based models. This approach has the potential to improve failure predictions, optimize performance, and reduce over-engineering, supporting more efficient and lightweight designs. This study presents the development and validation of a digital twin for a sensorized Unmanned Aerial Vehicle (UAV), focusing initially on a propeller boom arm mounted on a test rig for real-world testing in a controlled environment. The digital twin leverages both physics-based analysis provided by surrogate models of Autodesk Nastran and real-world sensor data. We perform a three-way comparison between Nastran, the digital twin, and sensor data to validate both the hardware and software setups, with ongoing efforts to reduce discrepancies and improve sensor placements. Our initial results highlight the potential of digital twins to significantly accelerate certification processes, reduce costs, and enable the faster adoption of new materials, ultimately driving innovation and transforming engineering practices across industries.

1. Background

In the rapidly evolving landscape of engineering certification, traditional methodologies are becoming increasingly inadequate as industries advance towards more innovative and high-performance designs. Existing certification workflows in fields such as automotive and aerospace rely heavily on factors-of-safety estimations and practices derived from historical data and physical testing, which can be costly and time-consuming [1]. Derivative methods, outlined in standards like NASA-STD-5001B [2], depend on archives of legacy data, which may not adequately address novel materials and designs emerging from advancements in structures and manufacturing techniques. Moreover, while test-based certification in standards like ASTM D3039/D3039M-17 [3] provide more accurate predictions of material behaviour through prototype testing, it is limited under specific environmental conditions and becomes inadequate for complex system interactions and greater variability in operating environments [4]. These methods prescribe conservative approaches–including factors of safety and prototype testing–often resulting in unnecessarily heavy structures that do not optimize performance or guarantee safety [4].

As engineers and designers explore innovative structures, materials, and manufacturing processes, current certification methods struggle to keep pace. This is particularly challenging when it comes to composites and additive-manufactured materials, as opposed to conventional materials like metals, where the behaviours are simpler, and engineers have decades of design experience. In contrast, newer materials which are gaining traction in lightweight applications due to their potential for enhanced performance, such as custom composite layups and lattice structures used in additive manufacturing, introduce complexities in predicting mechanical responses due to their unique geometries, anisotropic properties, and manufacturing process dependence [5, 6]. The speed at which new materials are being developed means there is limited historical data to guide safety assessments, making it difficult to accurately predict how these materials perform and age in real-world conditions. This lack of experience and understanding not only impedes the timely adoption of these innovative technologies but also creates inefficiencies in both design and certification workflows. Existing practices, which rely on conservative worst-case scenarios, fail to account for the nuanced failure modes of these materials, further hindering engineers from developing time-efficient, cost-effective, and certification-ready systems.

A promising solution to these challenges is the use of digital twins, which can transform how aerospace and automotive structures are designed, tested, and certified. By embedding sensors into designs during their operational phase, digital twins—virtual replicas of physical systems—can provide insights on

structural performance. In situ data collected through embedded sensors allows designers to better understand the performance of materials and structures throughout the product lifecycle, from initial design to end-of-life. This approach is particularly advantageous for advanced composite materials, where damage mechanisms are complex and less deterministic compared to traditional metals [7].

Digital twin approaches that leverage physics models [12, 13, 14] can further enable inference of quantities not directly measured by sensors, such as the stress and strain over the entire structure including locations not instrumented with sensors, or the unknown operating load conditions causing the structural response captured by the sensors. A digital twin, especially one that is capable of operating in real time, provides critical insight into how materials and structures behave under various loading conditions. It can enable advanced monitoring and diagnostics of the structure's health as it ages, anomaly and failure detection, as well as fatigue analyses based on the actual stress cycles of the structure. Moreover, operational insights gathered by digital twins, such as stress concentrations that may indicate potential failure points, provide valuable information to optimize future designs by reinforcing weak areas and reducing overengineered components, ultimately leading to lighter and more efficient structures. These capabilities allow a structure to operate safely during service without relying on limited experimental data and design knowledge, which can be particularly advantageous for anisotropic materials and parts with complex geometries whose behaviors are less well understood, and which traditional analyses struggle to model accurately. Modeling errors or model-form uncertainties in the digital twin due to simplifying assumptions in the physics simulation and uncertain aging effects can also be corrected based on sensor data using modal identification [15] and probabilistic model updating techniques [14, 16].

Despite the potential for digital twins to make the certification process more efficient, accurate, and adaptive to new materials and technologies, more research is required to make such digital twins a reality. Recent publications [12, 13, 17] have demonstrated the success of full-state inference from noisy and sparse sensor data. However, accurate and efficient inference of unknown operating conditions remains a challenge, especially without judicious prior model selection and tunning which is highly problem dependent. In addition, [14] proposed and demonstrated the viability of updating the digital twin model directly from in-situ data, even when the loading condition is unknown, but effectiveness of the approach remains to be proven in the presence of stronger model-form uncertainties when simulating structures made with advanced technologies. Moreover, a new digital-twin-enabled certification workflow must combine and streamline multiple algorithmic components. These include, for example, offline model preparation, training, and sensor placement, online inference and model updating, anomaly detection and fatigue analysis based on

the output of the digital twin, and an intelligent system which can inform future design of certification-ready structures; each of which requires different degrees of research and development to be ready for real-world engineering applications.

To move toward this goal, we have developed a research platform based on a multi-rotor Unmanned Aerial Vehicle (UAV). We start with a simple problem: a load-bearing propeller boom arm of the UAV, on which we set up a test rig to perform in-lab testing that mimic real-world mounting and load conditions. Our goal is to set up the sensor data gathering hardware and an initial digital twin software prototype based on existing approaches from literature. We aim to perform initial experiments and, more importantly, validation of the hardware and software to ensure reliable results. Thus, we begin by integrating sensors into an aluminum version of the boom arm in this paper and presentation, which will serve as a starting point for future work involving a composite boom and an additively manufactured UAV node connecting the arm to the rest of the UAV body. In parallel, we increase the complexity of the problem incrementally by focusing on relatively simple static and dynamic analyses on the test rig in this work before moving on to more complex behaviors of the arm and node during flight. We then incorporate failure analyses, such as fatigue prediction, in the future. This process will help us gain insights and scientific innovation to eventually transform the certification process.

This paper is more specifically organized as follows. Section 2 describes our UAV research platform, the test rig setup, and the hardware used for static and dynamic load experiments and localized strain data gathering. Section 3 presents our steps to create and validate the initial digital twin including: construction of a Nastran surrogate model for the boom arm, development of a digital twin algorithm which uses the surrogate model to translate localized strain data into a full distribution of the stress within the structure, and finally the experimental testing procedures to validate the sensor data as well as digital twin output. Section 4 presents some preliminary results towards verifying and validating the surrogate model, the digital twin algorithm, and the data gathering hardware.

2. Problem Description and Set Up

2.1 UAV Set Up

The UAV research platform designed and developed by the Autodesk Research team has a maximum take-off weight (MTOW) of 55pounds, or approximately 25 kg (Fig. 1). The UAV is a sensorized flying platform that functions as a testbed for our advanced CAD software development and novel scientific algorithms. It features four propeller arms, four landing gear legs, and a central body housing the battery, electrical components, and a front-mounted camera

inspection system. Its major dimensions are approximately 1.14 m in length, 1.14 m in width, and 0.66 m in height. We aim to eventually use this UAV to evaluate our digital twin algorithms subject to real-world conditions and investigate how data and insights gathered using the digital twin can enable more performant and certification-ready structural design of the UAV.

Figure 1: CAD image of the Autodesk 55-pound MTOW UAV

2.2 Test Rig Setup

The test rig, modeled after the 55-pound MTOW UAV, consists of a single UAV propeller boom arm, boom socket, propeller motor, and the corresponding motor housing and mounts, along with a stationary mount replicating the connection to the UAV body (Fig. 2). The boom arm, which connects the propeller motor to the UAV socket, is a load-carrying member for which we wish to create an experimental digital twin. The motor housing and attachments are additively manufactured, and the motors are replaced with precision-machined weights matching the motors' mass, allowing for loading and testing without damage to electrical components of the actual motor. The work-holding mount of the test rig is a precision-machined stand that enables the entire propeller arm system to rotate in 22.5-degree intervals, allowing the boom arm to be loaded at various angles.

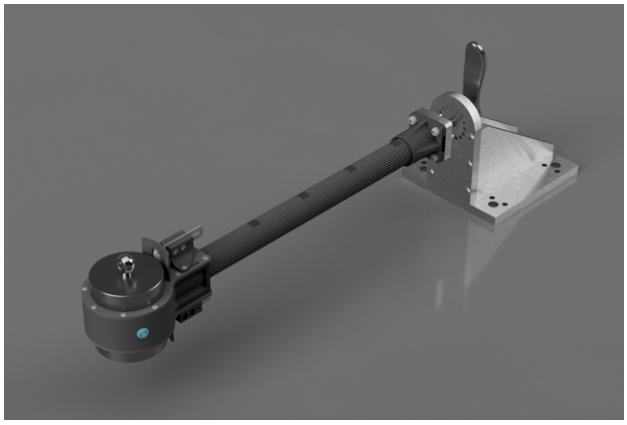

Figure 2: Design of the UAV motor boom test rig

2.3 Data Gathering Setup

The test rig is loaded statically and dynamically using both the Instron 6800 series machine and the Universal Robot UR10e collaborative robot. The Instron 6800 series is a universal testing system designed for tensile, compression, and flexure testing (Fig. 3). It enables precise load application with high accuracy, featuring a 5 kHz data acquisition rate and 0.5% accuracy down to 1/1000th of the load cell's capacity [8]. Using the Instron, we can apply controlled loads to the test rig while monitoring force, displacement, and time series data in real time.

Figure 3: Instron 6800 series universal testing system

The UR10e collaborative robot, a medium-duty robot with sensorized joints, is used for randomized load applications on the test rig (Fig. 4). With a reach of 1300 mm and a maximum payload of 12.5 kg [9], the UR10e introduces dynamic, unknown loads to the system after the digital twin algorithm has been verified with the controlled loads applied by the Instron. This allows for testing on the algorithm's ability to infer loads under varying unknown load conditions, more closely mimicking the unknown load quality in flight.

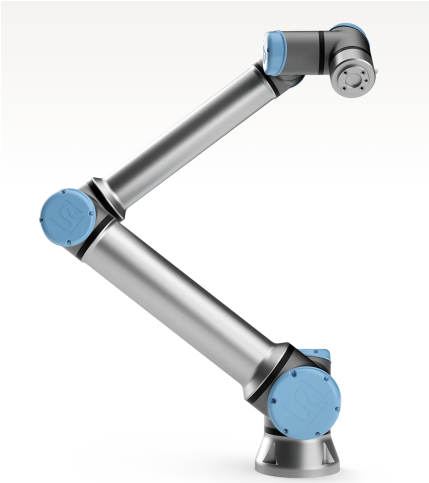

Figure 4: UR10e collaborative robot

The boom arm is instrumented with strain gauges for monitoring the strain during testing. Strain data is collected using a Labjack T7 analog extension board [10], which interfaces with full bridge strain gauges (N2A-06-S5139U-350/E4) mounted on the boom arm of the test rig. These strain gauges, with a resistance of 350 ohms and a gauge factor of 2.05 [11], are strategically placed along the boom arm's outer surface in alignment with the boom's direction. After calibration, the strain gauges provide localized strain data. The strain is calculated using the full bridge strain gauge equation,

$$\varepsilon = \mathrm{V}_{out} \cdot V_{in} \cdot \mathrm{GF}, \tag{1}$$

where V_{out} is the difference between the stressed and resting voltages (in volts), V_{in} is the input voltage (in volts), GF is the gauge factor, and ε represents the strain.

By combining the precise control of the Instron system and the dynamic load applications from the UR10e, along with the strain measurements using full bridge sensors and Labjack T7 signal processing, this setup enables comprehensive testing of the digital twin algorithm's performance under a range of load conditions.

3. Digital Twin Development and Validation

Our goal is an initial digital twin of the boom that takes as input sparse strain data and outputs a full reconstruction of the stress field within the structure. We develop and validate this digital twin via the following three-part process:

Part 1 (Section 3.1) constructs a surrogate model for the finite element analysis (FEA) of the boom arm using Autodesk Nastran. The surrogate model simulates the arm's response to the applied load in real-time and provides a physics-based relationship between the load and the stress and strain throughout the boom, which is needed by the digital twin algorithm.

Part 2 (Section 3.2) develops a digital twin of the boom using the surrogate model from Part 1 and strain gauge data gathered from the physical boom. This provides real-time insights into the behavior of the boom without assuming prior or immediate knowledge of the operating conditions, hence has the potential to address some of the certification challenges outlined in Section 1.

Part 3 (Section 3.3) performs a three-way validation between Nastran, the digital twin algorithm from Part 2, and the physical data gathered by the sensors for a series of experiments using the Instron machine and the UR10e. This allows us to establish the quality of the sensor data, and the digital twin output comparison will ensure the accuracy of the simulation and the digital twin.

3.1 Surrogate Model

In part 1 of this work, we develop a surrogate model for Nastran in Python. This step is needed because Nastran, although powerful, is too computationally intensive to be used directly in the digital twin for real-time reconstruction of the stress field. Therefore, we aim to create a surrogate model of Nastran that is significantly smaller in size, allowing for faster, real-time computation, while maintaining acceptable accuracy. We create separate surrogate models respectively for the static and dynamic simulation of the aluminum boom in Nastran. Each surrogate model takes as input an arbitrary static or dynamic load applied at the motor's center of mass, and produces as output the static or dynamic displacement, stress, and strain across the entire structure (Fig. 5). This surrogate model will serve as a key component in the digital twin algorithm described in Section 3.2.

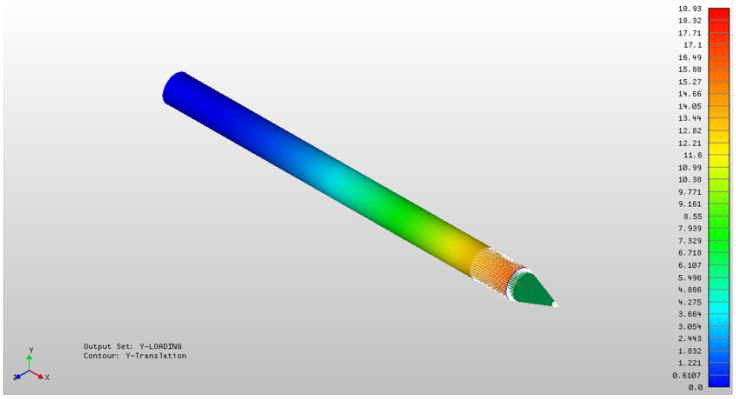

Figure 5: CAD configuration for surrogate model development

For static load cases, we utilize the principle of superposition, which states that the solution to a linear static problem can be found by summing the individual contributions of various loads. In the context of our system, the displacement u is the solution the equation,

$$Ku = f,$$

where K is the stiffness matrix, u is a vector of all unconstrained nodal displacements, and f is the vector of external load applied at each node.

For our application, f represents the resultant nodal force vector generated by applying an arbitrary load at the motor's center of mass. We express this arbitrary load a weighted sum of three unit forces and moments in the x, y, and z directions, or a sum of six unit loads applied to the motor's center of mass (Fig. 6).

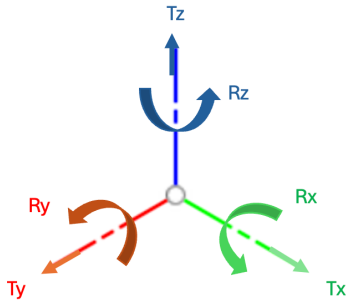

Figure 6: Six Degrees of Freedom (DOF) indicating direction of all unit loads

We then have

$$f = \sum_{i=1}^{6} \alpha_i f_i,$$

where f_i represents the nodal force vector from applying a unit force in one of the six directions indexed by i, and α_i is the load magnitude in the i-th direction. By applying the principle of superposition, the total displacement u can be expressed as:

$$u = \sum_{i=1}^{6} \alpha_i u_i,$$

where u_i is the displacement response due to each unit force f_i. This allows us to compute the displacement for any arbitrary load.

We apply the same principle of superposition to obtain an expression for the stress and strain. We denote the stress and strain produced by the unit force f_i as σ_i and ε_i respectively. The stress σ and strain ε at any location in the structure due to an arbitrary multidirectional force, *f*, is then given by

$$\sigma = \sum_{i=1}^{6} \alpha_i \sigma_i \,, \tag{2}$$

$$\varepsilon = \sum_{i=1}^{6} \alpha_i \epsilon_i \,. \tag{3}$$

To construct the surrogate model, we simulate each of the six unit loads f_i using Nastran. We then extract from the Nastran output files the corresponding nodal displacement u_{i}, elemental stress σ_{i}, and elemental strain ε_{i} for each unit load, and store them as NumPy arrays for efficient computation.

For linear dynamic load cases, we construct the surrogate model using modal analysis. The equation of motion for a specific mode *k* undergoing vibration analysis is defined by:

$$\ddot{q_k}(t) + 2\zeta_k \omega_k \dot{q}_k(t) + \omega_k^2 q_k(t) = V_k^T f(t) \tag{4}$$

where $q_k(t)$ is the generalized coordinates for the *k*-th mode with time derivatives $\dot{q}_k(t)$ and $\ddot{q}_k(t)$, ζ_k is the modal damping ratio for the *k*-th mode, ω_k^2 is the squared natural frequency of the *k*-th mode, $f(t)$ is the external force vector applied to the system at time *t*, and $V_k^T f(t)$ is the projection of the external force $f(t)$ onto the *k*-th mode shape, representing the effective force experienced by the *k*-th mode.

To determine the right-hand side of equation (4), we express $f(t)$ again as a weighted sum of six unit loads f_i with time-dependent magnitudes $\alpha_i(t)$:

$$f(t) = \sum_{i=1}^{6} \alpha_i(t) f_i.$$

Substituting the above into the right-hand side of equation (4) leads to

$$V_k^T f(t) = \sum_{i=1}^{6} \alpha_i(t) V_k^T f_i \,, \tag{5}$$

as the effective external force for the k-th mode. Given six time-dependent load magnitudes $\alpha_i(t)$ for the six unit loads, we evaluate the surrogate model by approximating the major modal contributions to the six degrees of freedom by solving m modal equations subject to the dynamic load in equation (5). We then compute the resulting displacement $u(t)$, strain $\varepsilon(t)$, and stress $\sigma(t)$ using the natural mode shape V_k, strain ϵ_k, and stress σ_k associated with each of the m modes as follows:

$$u(t) = \sum_{k=1}^{m} q_k(t) V_k,$$
$$\varepsilon(t) = \sum_{k=1}^{m} q_k(t) \epsilon_k,$$
$$\sigma(t) = \sum_{k=1}^{m} q_k(t) \sigma_k.$$

We create the surrogate model by extracting the mode shapes and natural frequencies from the Nastran simulation results. This involves selecting the m most significant modes based on their modal effective mass contributions to the system to capture the largest portion of the system's response. Once the natural modes are identified, the corresponding stress and strain distribution for each mode are also extracted.

3.2 Digital Twin Algorithm

In part 2 of this work, we develop digital twin algorithms to reconstruct the full stress field response within the structure based on strain data gathered by one or more sensors on the boom, without assuming knowledge of the load (i.e., the α_i's introduced previously). We again consider the static load and dynamic load cases separately, making use of the surrogate models described in Section 3.1.

For static load cases, we solve a linear least squares problem to obtain the unknown load magnitudes α_i, $i = 1, \ldots, 6$, based on the strain measurements; we then use equation (2) to evaluate the elemental stress σ resulting from the applied load. We simplify the notations herein by introducing a vector

$$\alpha = [\alpha_1, \alpha_2, \alpha_3, \alpha_4, \alpha_5, \alpha_6]^T,$$

to describe the unknown applied load. To set up the least squares problem, we gather all strain measurements y_j into a vector

$$y = \left[y_1, y_2, \cdots, y_{n_o}\right]^T,$$

where n_o is the number of sensors on the boom. We also gather the elemental strain for all six unit loads into an n-by-6 matrix,

$$\mathcal{E} = [\epsilon_1, \epsilon_2, \epsilon_3, \epsilon_4, \epsilon_5, \epsilon_6],$$

where n is the size of each $\epsilon_i,\ i = 1, \cdots, 6$, is the element strain resulting from the application of unit load f_i. Since we model the boom arm using shell analysis in Nastran, there are 3 stress and strain components per element, so n is 3 times the number of elements. Let ϵ be the elemental strain associated with the unknown applied load, and $H \in \mathbb{R}^{n_o \times n}$ be a measurement matrix such that

$$y = H\epsilon,$$

then the least of squares problem we aim to solve can be expressed as

$$\alpha^\star = \underset{\alpha}{\operatorname{argmin}}\ \|y - H\mathcal{E}\alpha\|_2^2, \tag{6}$$

where $\alpha^\star$ is the least-squares estimate of the unknown load magnitude based on the strain measurements.

For dynamic load cases, we adopt the approach in [13,17] which is based on Kalman filtering and a Gaussian process latent force model for the unknown load. We describe the unknown dynamic load via the vector function

$$\alpha(t) = [\alpha_1(t), \alpha_2(t), \cdots, \alpha_6(t)]^T.$$

We first formulate the equations of motion in (4) and (5) for the m modes into the following state space model for a first-order dynamical system:

$$\dot{x}(t) = A_c x(t) + B_c \alpha(t), \tag{7}$$

where x contains the generalized coordinates $q_k(t)$ from (4) and their respective time derivatives $\dot{q}_k(t)$:

$$x(t) = [q_1(t), q_2(t), \cdots, q_m(t), \dot{q}_1(t), \dot{q}_2(t), \cdots, \dot{q}_m(t)]^T,$$

A_c and B_c are derived by rewriting equation (4) for the m modes as a system of first-order ordinary differential equations:

$$A_c = \begin{bmatrix} 0 & I \\ -\begin{bmatrix} \omega_1^2 & & \\ & \ddots & \\ & & \omega_m^2 \end{bmatrix} & -\begin{bmatrix} 2\zeta_1\omega_1 & & \\ & \ddots & \\ & & 2\zeta_m\omega_m \end{bmatrix} \end{bmatrix},$$

$$B_c = \begin{bmatrix} 0 \\ -\begin{bmatrix} V_1^T f_1 & \cdots & V_1^T f_6 \\ \vdots & \ddots & \vdots \\ V_m^T f_1 & \cdots & V_m^T f_6 \end{bmatrix} \end{bmatrix}.$$

We additionally express the dynamic strain measurements $y(t)$ in terms of $x(t)$ via

$$y(t) = G_c x(t),$$

where

$$G_c = \begin{bmatrix} [H\epsilon_1, H\epsilon_2, \cdots, H\epsilon_m] \\ 0 \end{bmatrix},$$

and ϵ_k, $k = 1, \cdots, m$, is the elemental strain associated with the k-th mode.

If we know $x(t)$ at time 0 and the load magnitudes in $\alpha(t)$, we can in theory use equation (7) to predict the state of the system at any future time and evaluate the stress distribution within the boom. However, this does not in practice produce an accurate digital twin of the physical system (the boom arm in this case) because equation (7) is not a perfect model, which causes the predicted $x(t)$ to deviate over time from the physical reality, and we often do not know $\alpha(t)$. The approach in [13, 17], which we refer to as KF-GPLFM, allows us to obtain a more accurate estimate of $x(t)$ based on the strain data measured by the sensors on the boom.

We omit the full detail of KF-GPLFM since it is well documented in [13, 17], but the idea to model the unknown function $\alpha(t)$ as a Gaussian process formulated as a secondary state space model similar to equation (7). We form an augmented system describing the time evolution of $x(t)$ and $\alpha(t)$ by appending the state space model for $\alpha(t)$ to equation (7). We can then apply Kalman filtering to the augmented system to obtain estimates of $x(t_j)$ for incremental time values t_j based on state and input estimates $x(t_{j-1})$ and $\alpha(t_{j-1})$ from a previous time value t_{j-1} as well as the new sensor measurements $y(t_j)$ from the current time t_j.

3.3 Validation Between Physical Data, Nastran, and Digital Twin

To establish a three-way agreement between physical sensor data, Nastran simulation data, and the digital twin, both static and dynamic tests are

conducted physically and digitally. Both static and dynamic load testing involves applying a point load using the Instron machine to the sensorized test rig. Force and strain data are collected over time using the Instron machine and strain gauges, respectively. This data is then cleaned and compared with the Nastran simulation results. To validate the digital twin, we assume no knowledge of the unknown load and instead infer it from a subset of the sensor measurements gathered from the boom arm. We then compare the inferred load and stress distribution against the actual applied load and the strain measurements from the remaining sensors (which are not used during inference), as well as the Nastran simulation.

We perform the static tests by applying a point load downward at varying forces on the propeller end of the test rig using the Instron. We then rotate entire propeller arm system (about the axis aligned with the length of the boom) using the work-holding mount of the test rig, and repeat the same loading (Fig. 7).

Figure 7: Instron sensor test rig loading setup

For each load case and test rig orientation, a corresponding Nastran simulation is run. The Nastran model represents the physical setup with the boom socket receiver as a solid part, the aluminium boom as a shell idealization using a quadrilateral mesh, and the motor as a rigid point mass, including the centre of gravity, principal moments of inertia, and weight (Fig. 8). The forces applied by the Instron are modelled as remote forces acting on the system at the approximated point of contact between the load application machine and the motor of the propeller.

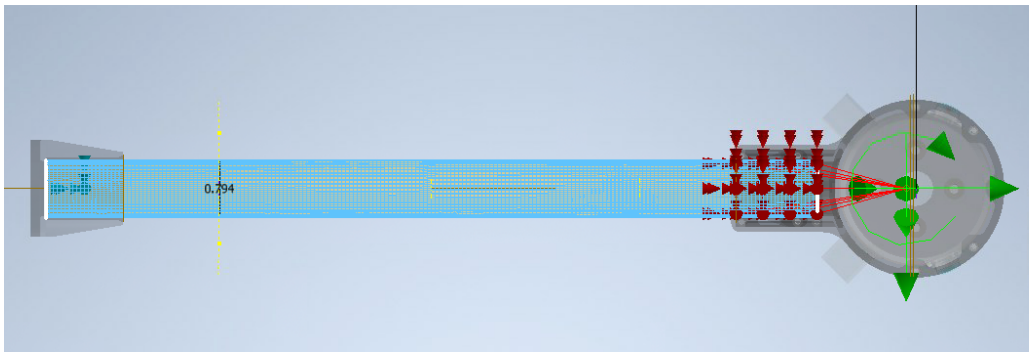

Figure 8: Nastran Test Rig Simulation Setup

Elemental strain data is extracted from the Nastran model at locations corresponding to the physical strain gauges. These Nastran strain values are then compared to the physical sensor data to assess agreement. Similarly, displacement data collected from the Instron machine is compared with the corresponding Nastran displacement data. This comparison establishes a baseline, confirming reasonable agreement between the FEA simulations and the physical setup. This increases confidence in the accuracy of both the simulation and the test rig before progressing to more complex dynamic loading tests.

For dynamic loading, a sinusoidal load is applied downward at varying forces on the propeller end of the test rig. As with static testing, the test rig is rotated to different angles, and the loading is repeated. To avoid resonance, the load frequency is intentionally kept away from the system's natural frequencies. This prevents the excitation of overly simple sinusoidal modes, which could be too predictable and fail to provide meaningful insights. The same dynamic sinusoidal load is then applied to the corresponding Nastran simulation, following the same procedure as in static testing. Elemental strain is again probed in the Nastran model at locations corresponding to the physical strain gauge placements. The same simulation is then repeated using the Nastran surrogate model described in Section 3.1. By comparing the data from the physical sensors, Nastran simulation, and the surrogate model, we can evaluate the error introduced by modal reduction and validate the system’s accuracy. This comparison helps us identify and understand any discrepancies between the three models. Once agreement is established between the physical data and simulation results, we proceed to validate the digital twin algorithm by inferring the unknown load and stress distribution based on localized sensor measurements.

Finally, we perform more complex dynamic and torsional load tests using the UR10e robot, where the loads will represent unknown external forces acting on the system. These tests provide a demonstration of the digital twin algorithm’s inference accuracy and its real-time performance.

4. Preliminary Results

At the time of writing this paper, we have just gathered the first set of Instron test data towards the three-way validation between the strain gauge measurements, Nastran, and the digital twin algorithm described in Section 3.3. This section thus provides some very early results which we intend to improve upon. Section 4.1 verifies the correctness of the surrogate models in Section 3.1. Section 4.2 demonstrates some initial digital twin results based on synthetic data as a temporary placeholder until the actual strain data is validated and ready to be used as input to the digital twin. Section 4.3 provides the initial validation results between Nastran and the Instron test data. We aim to provide additional results during the presentation as our work progresses.

4.1 Surrogate Model Verification

For static loading, we verified the displacement, stress, and strain produced by the surrogate model via the principal of superposition by comparing them against the output of a Nastran simulation for an arbitrary test load with magnitudes $\alpha = [1, 1, 1, 1, 1, 1]^T$. The relative error in the stress, given by

$$\text{relative stress error} = \frac{\sqrt{\sum_{i=1}^{n}(\sigma_{1i} - \sigma_{2i})^2}}{\sqrt{\sum_{i=1}^{n}\sigma_{2i}^2}}, \tag{8}$$

where n is the number of elements in the model, σ_1 is the inferred stress vector from the surrogate model, and σ_2 is the stress vector from the Nastran simulation, is found to be of magnitude approximately 10^{-6}. Similarly, the relative error in the displacement error, given by

$$\text{relative displacement error} = \frac{\sqrt{\sum_{i=1}^{n}(u_{1i} - u_{2i})^2}}{\sqrt{\sum_{i=1}^{n}u_{2i}^2}}, \tag{9}$$

where n is the number of nodes in the model, u_1 is the inferred displacement vector from the surrogate model, and u_2 is the actual displacement vector from the Nastran simulation, is found to be of magnitude approximately 10^{-7}. From verifying that the results of equations (8), and (9) are close to zero, the surrogate model for static loading is validated to be correct.

For dynamic loading, we ensured that the natural mode shapes V_k and the natural frequencies ω_k in equation (4) are parsed correctly from the Nastran output. We do so by verifying the following:

$$\frac{\|V^T K V - \mathrm{diag}(\Omega)\|}{\|\Omega\|} \approx 0, \tag{10}$$

where V is a matrix containing the first 100 modes shapes, i.e., V_k, $k = 1, \cdots, 100$, as columns, K is the global stiffness matrix of the system output by Nastran, Ω is a vector containing the first 100 eigenvalues, i.e., ω_k^2, $k = 1, \cdots, 100$, and $\mathrm{diag}(\Omega)$ is a diagonal matrix with Ω as the diagonal. We also verify the following:

$$\|V^T M V - I\| \approx 0, \tag{11}$$

where M is the global mass matrix output by Nastran and I is the identity matrix. Our results confirmed that both (10) and (11) are true to the order of 10^{-7}, verifying that we have the correct modal decomposition for the surrogate model for dynamic loading.

4.2 Initial Digital Twin Results

4.2.1 Digital Twin for Static Loads

As an initial demonstration of the digital twin algorithm for static loads in Section 3.1, we generate synthetic strain data based on a Nastran simulation for an arbitrary test load with magnitudes $\alpha = [1, 1, 1, 1, 1, 1]^T$. We then assume that the value of α is not known and infer it based on a small number of synthetic strain measurements using equation (6).

We experimented with the sensor placement strategy outlined by Manohar et al. [18]. The strategy is based on Pivoted QR (PQR) factorization of the matrix $H\mathcal{E}$ in equation (6), which computes

$$(H\mathcal{E})P = QR,$$

where $H\mathcal{E}$ is a 6 by n matrix, where the 6 rows correspond to the strains in each unit load direction, and n is 3 times the number of elements, accounting for elemental strains in the x, y, and shear directions. Q is a 6 by n orthogonal matrix, where the columns of Q are orthogonal, and R is an upper triangular matrix of size n by n. Performing QR pivoting in python gives us the P vector, an n by 1 permutation vector that represents the reordering of columns (pivoting) during the decomposition, giving us the ranking of the optimal sensor locations and directions.

To understand the efficiency of PQR sensor locations (Fig. 9) at making inferences on the rest of the system, a consequent number of sensor locations

are arbitrarily chosen spaced evenly along the boom with varying mounting directions for comparison (Fig. 10).

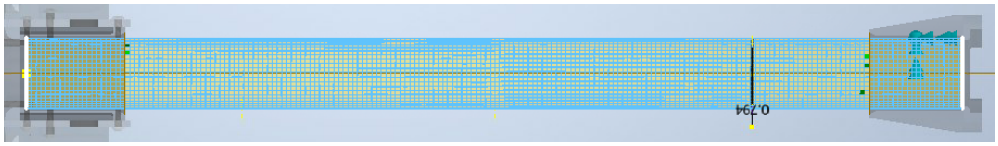

Figure 9: PQR sensor locations along the boom

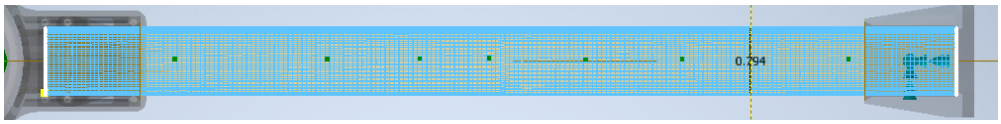

Figure 10: Arbitrary sensor locations along the boom

By extracting the strain values at corresponding PQR and arbitrary sensor locations, we use equation (6) to solve for inferred load magnitudes given the varying number of sensors and locations. The relative load magnitude error is calculated based on the following metric:

$$\text{relative load magnitude error} = \frac{\sqrt{\sum_{i=1}^{6}(\alpha_{1i} - \alpha_{2i})^2}}{\sqrt{\sum_{i=1}^{6}\alpha_{2i}{}^2}},$$

where α_1 is the inferred load magnitude vector using equation (6), and $\alpha_2 = [1,1,1,1,1,1]^{\mathrm{T}}$ is the actual load magnitude vector used by the Nastran simulation. The resultant relative errors given varying number of sensors for PQR, and arbitrary sensor locations are plotted in Fig. 11.

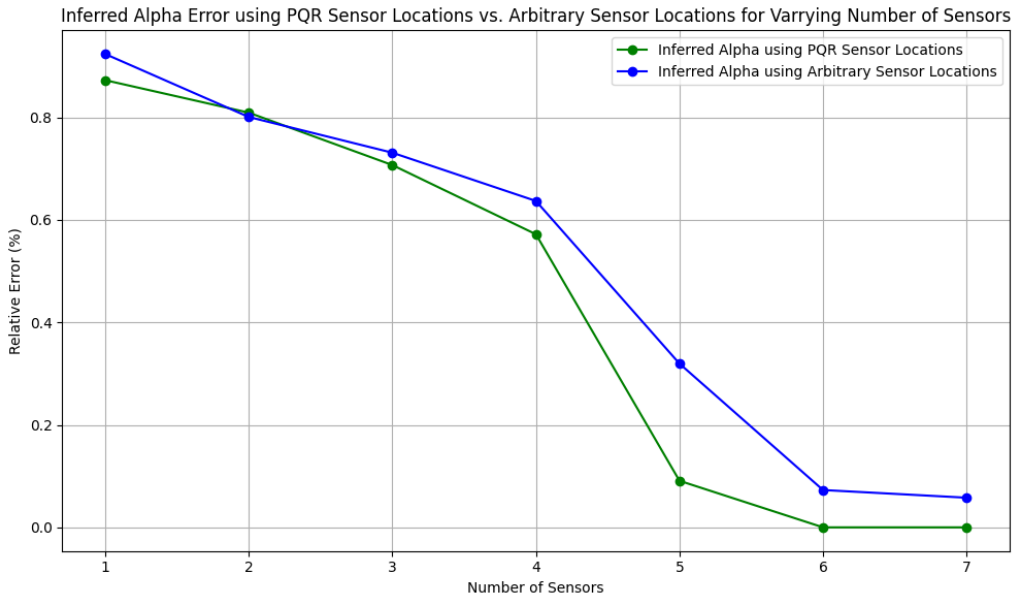

Figure 11: Table comparing inferred alpha error between PQR and arbitrary sensor locations for various number of sensors

By comparing the different sensor variables, we can observe the effect that various numbers of PQR sensor locations have on reducing the relative error in load magnitude inference of the digital twin. Most significantly, the PQR sensor placement reduces relative error down to 0.009% when using 5 sensors, which is 251.07% more accurate compared to the relative error of 5 arbitrary sensor locations.

4.2.2 Digital Twin for Dynamic Loads

We assess the system's dynamic characteristics by computing the first 1500 natural modes of the system. The cumulative sum of the percent modal effective mass against the number of modes is plotted in Fig. 12 for each of the 6 nodal degrees-of-freedom (DOF). The percent modal effective mass indicates how much each mode contributes to the system's overall dynamic behavior. To select the modes for the surrogate model, we identify 18 modes with a percentage modal effective mass of at least 1% for any nodal DOF. We remove 4 of the 18 modes whose natural frequency is more than 50 times the lowest natural frequency to ensure the dynamical system is not too stiff numerically. The remaining 14 modes are used to generate the digital twin results in this section.

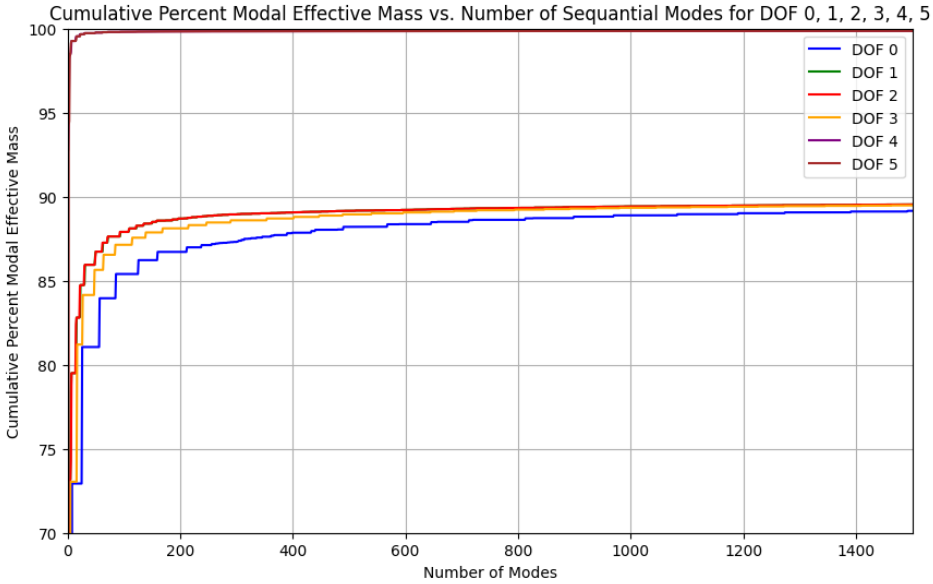

Figure 12: Cumulative percent modal effective mass for all DOF

To generate the synthetic sensor data, we apply a dynamic load with magnitudes

$$\alpha(t) = \begin{bmatrix} 0.18126989 \\ 0.15373705 \\ 0.08891329 \\ 0.07566059 \\ 0.13601713 \\ 0.04245141 \end{bmatrix} \sin(21882.17t).$$

We also introduced Rayleigh damping with a mass coefficient of 0.1 and stiffness coefficient of 0.0005. For the preliminary results, we assume to have sensor measurements for the y displacement (DOF 1) at Node 2930 (near the motor in Fig. 12) for $t = [0,\ 0.0091]$ seconds, sampled at approximately 1MHz, and is corrupted by Gaussian white noise with a covariance of 3.66×10^{-10}. The synthetic displacement data is used to infer the displacements for the rest of the boom arm using the digital twin approach in Section 3.2, while assuming that $\alpha(t)$ is unknown. Fig. 14 shows the time history of the synthetic displacement data, as well as the inferred values of the measured displacement and the unobserved displacements for all nodal DOFs at Node 2942 (near the fixed end of the boom arm in Fig. 13). Fig. 14 also shows the "ground truth" which is the actual uncorrupted displacement at these nodes from the original dynamic simulation for comparison. Figures in the first column of Fig. 15 present an example visualization of the inferred displacement field over the entire boom arm at 3 different time values. Figures in the second column of Fig. 15 show the deformed shapes of the boom (scaled up by a factor of 1000) based on the inferred displacement field superimposed

on the actual deformed shape based on the original simulation. The preliminary results in Figs. 14 and 15 suggest that it is possible to infer the full dynamic state of a structural system based on a single localized sensor measurement.

For the presentation, we aim to present similar results using actual strain measurements taken during dynamic load testing with the Instron and UR10e.

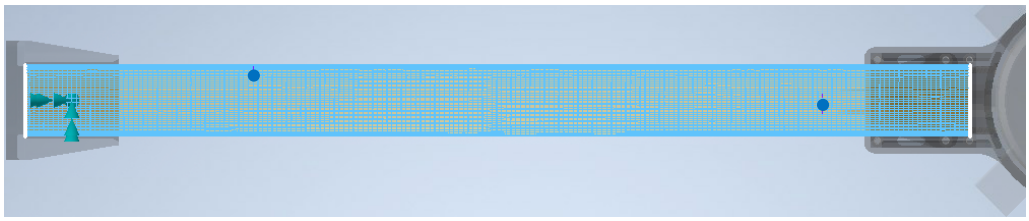

Figure 13: Sensor measurement locations

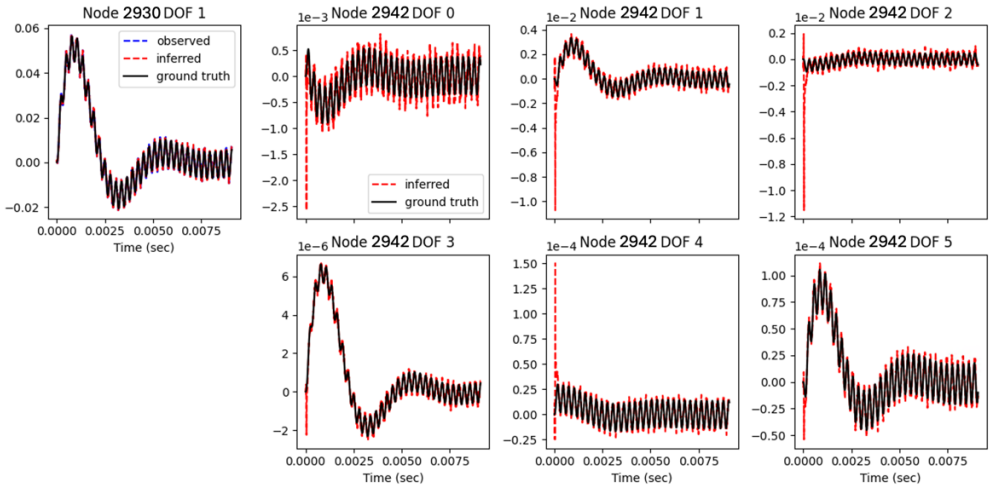

Figure 14: Time histories of the synthetic displacement measurements (top left) at Node 2930 and the inferred displacements for the 6 nodal DOFs at node 2342.

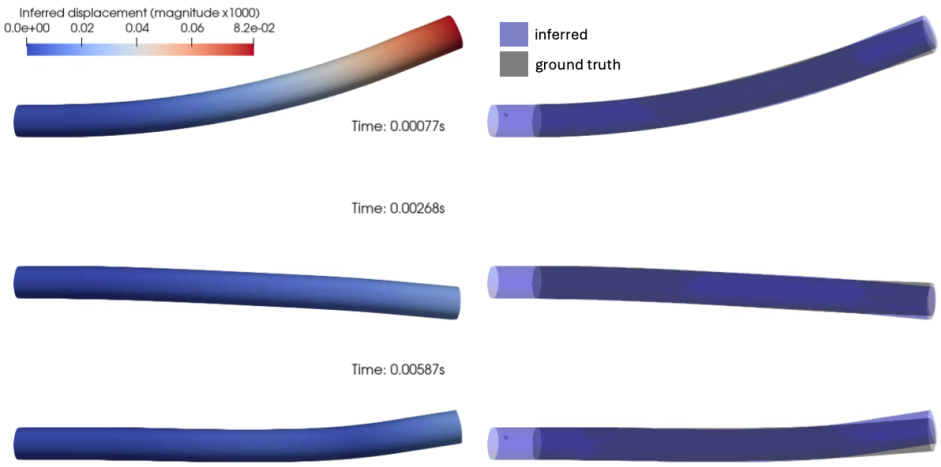

Figure 15: Deformed shapes of the boom arm at different time values based on the inferred displacement field.

4.3 Nastran and Physical Data Validation Results

Initial Instron testing at various loads and directions are described in Table 1.

Table 1: Instron Static Load Experiment Setup

Loading Configuration	Maximum Force Applied (N)	Angle of Test Rig (°)
1	50.06	0
2	100.04	0
3	150.01	0
4	250.02	0
5	50.08	180
6	100.04	180
7	150.01	180
8	250.04	180
9	50.03	90
10	100.05	90
11	150.07	90
12	250.07	90
13	50	270
14	100.02	270
15	150.06	270
16	250.06	270
17	50.02	45
18	100.04	45
19	150.03	45
20	250.06	45
21	50.03	225
22	100.01	225
23	150.05	225
24	250.07	225

From the testing configurations described, the Instron vertical displacement and strain readings are calculated using equation (1) from recorded strain gauge voltages during physical testing, while the corresponding strain and displacement at the same locations are extracted from Nastran simulations. Initial data and relative error results are generated for loading configurations 1 to 4, for the two strain gauge positions mounted along the length of the boom, as shown in Fig. 16. The initial displacement results from Instron and Nastran are listed in Table 2, and the strain results at strain gauge positions 2 and 3 are calculated in Table 3. Larger discrepancies are observed as the load increases. We intend to further investigate the cause of these errors for the presentation.

Figure 16: Configuration of strain gauge positions, mounting in line with indicated arrow

Table 2: Maximum Displacement and Relative Error for Various Loading Configurations

Loading Configuration	Instron Compressive Displacement at Maximum Force (mm)	Nastran Displacement (mm)	Relative Displacement Error (%)
1	1.28	1.18	8.69%
2	2.63	2.00	31.59%
3	4.02	2.82	42.59%
4	6.84	4.46	53.28%

Table 3: Strain Readings and Sensor Locations

Loading Configuration	Instron Strain Reading		Nastran Strain Reading		Relative Error at Sensor Locations (%)	
	2	3	2	3	2	3
1	6.0E-05	1.0E-04	5.8E-05	9.1E-05	3.90%	13.59%
2	1.4E-04	2.1E-04	9.7E-05	1.5E-04	40.76%	38.20%
3	2.5E-04	2.9E-04	1.4E-04	2.2E-04	81.31%	32.98%
4	3.3E-04	4.9E-04	2.2E-04	3.5E-04	50.44%	40.60%

5. Conclusion

The aerospace and automotive industries are increasingly challenged by traditional certification workflows, which struggle to keep pace with new materials like composites and additive manufacturing. These materials have complex failure mechanisms that current certification methods, relying on conservative safety factors and physical testing, cannot efficiently address. As a result, engineers face barriers to fully utilizing the potential of novel materials and structures.

Digital twins offer a promising solution by providing real-time performance insights through virtual replicas of physical systems. These models, combined with sensor data, enable better failure prediction, fatigue analysis, and structural monitoring, particularly for complex materials. Preliminary results in our work on a sensorized test rig for an UAV propeller arm has demonstrated the potential in our digital twin algorithm to quickly and accurately infer system properties based on limited synthetic data. We have successfully developed static and linear dynamic FEA surrogate models for the digital twin algorithm using Autodesk Nastran and are working on refining the digital twin algorithm to improve predictions and minimize discrepancies with simulation and experimental data.

Future work will focus on optimizing sensor placement, reducing data noise, and improving model accuracy to better simulate real-world conditions. By addressing current challenges in data integration and model refinement, we aim to develop a robust digital twin-based certification process that can expedite material adoption, reduce costs, and enable more adaptive, reliable engineering workflows. Ultimately, this approach has the potential to revolutionize certification, driving innovation across industries.

6. References

[1] Grieves, M., “Digital Twin Certified: Employing Virtual Testing of Digital Twins in Manufacturing to Ensure Quality Products,” Machines, Vol. 11, No. 8, 2023, pp. 808. https://www.mdpi.com/2075-1702/11/8/808

[2] NASA, “NASA-STD-5001B: Structural Design and Test Factors of Safety for Spaceflight Hardware,” NASA Standards, 2022.

[3] ASTM, “ASTM D3039/D3039M-17: Standard Test Method for Tensile Properties of Polymer Matrix Composite Materials,” ASTM International, West Conshohocken, PA, 2017.

[4] Glaessgen, E. and Stargel, D., “The Digital Twin Paradigm for Future NASA and US Air Force Vehicles,” in *53rd AIAA/ASME/ASCE/AHS/ASC Structures, Structural Dynamics and Materials Conference*, Honolulu, Hawaii, 23-26 April 2012, p. 1818. https://doi.org/10.2514/6.2012-1818

[5] Maes, V. K., Potter, K., and Kratz, J., “Features and Defects Characterisation for Virtual Verification and Certification of Composites: A Review,” *Composites Part B: Engineering*, Vol. 246, November 1, 2022, Article 110282. https://research-information.bris.ac.uk/en/publications/features-and-defects-characterisation-for-virtual-verification-an

[6] Almalki, A., Downing, D., Lozanovski, B., Tino, R., Du Plessis, A., Qian, M., Brandt, M., and Leary, M., “A Digital-Twin Methodology for the Non-Destructive Certification of Lattice Structures,” *JOM*, Vol. 74, No. 4, April 2022, pp. 1784–1797. https://link.springer.com/article/10.1007/s11837-021-05144-5

[7] M. G. R. Sause, E. Jasiūnienė, and R. Pullin, "Chapter 1, Introduction," in *Structural Health Monitoring Damage Detection Systems for Aerospace*, M. G. R. Sause and E. Jasiūnienė, Eds., Springer Aerospace Technology, 2021.

[8] INSTRON, “6800 SERIES Universal Testing System for Tensile, Compression, and Flexure Testing,” *INSTRON*. https://www.instron.com/en/products/testing-systems/universal-testing-systems/low-force-universal-testing-systems/6800-series?utm_feeditemid=&utm_device=c&utm_term=&utm_source=google&utm_medium=ppc&utm_campaign=Leads-Performance+Max-1&hsa_cam=22114671034&hsa_grp=&hsa_mt=&hsa_src=x&hsa_ad=&hsa_acc=4977827209&hsa_net=adwords&hsa_kw=&hsa_tgt=&hsa_ver=3&gad_source=1&gclid=EAIaIQobChMIiqrR1caJiwMV39XCBB1j_R7TEAAYASAAEgL7FfD_BwE (accessed Jan. 30, 2025).

[9] UNIVERSAL ROBOTS, “UR10e,” *UNIVERSAL ROBOTS*. https://www.universal-robots.com/products/ur10e/?utm_source=Google&utm_medium=paid-search&utm_campaign=HQ_Direct_paid-search_Google_2024-1-29_NAM%20Always%20On&utm_content=Direct-Direct&utm_campaign_id=701P4000007MsaSIAS&gad_source=1&gclid=EAIaIQobChMI7aes0M2JiwMVOSKtBh11LBlJEAAYAiAAEgLHUfD_BwE (accessed Jan. 30, 2025).

[10] LabJack, “LabJackT7,” *LabJack Measurement & Automation*. https://labjack.com/products/labjack-t7?srsltid=AfmBOorECClUP3Qad7T9rFKr0zpg1ayilaxh0Q13qu8CdXQjCbPPkQh1 (accessed Jan. 30, 2025).

[11] MicroMeasurements, “S5139,” *MicroMeasurements A VPG Brand*. https://www.micro-measurements.com/pca/detail/s5139 (accessed Jan. 30, 2025).

[12] S. E. Azam, E. Chatzi, C. Papadimitriou, “A dual kalman filter approach for state estimation via output-only acceleration measurements,” *Mechanical systems and signal processing* vol. 60, pp. 866–886, Aug. 2015, doi: https://doi.org/10.1016/j.ymssp.2015.02.001.

[13] S. Vettori, E. D. Lorenzo, B. Peeters, and E. Chatzi, “Assessment of alternative covariance functions for joint input-state estimation via Gaussian Process latent force models in structural dynamics,” *Mechanical Systems and Signal Processing*, vol. 213, pp. 111303–111303, Mar. 2024, doi: https://doi.org/10.1016/j.ymssp.2024.111303.

[14] Z. J. Zhang *et al.*, “Probabilistic Learning from Real-World Observations of Systems with Unknown Inputs for Model-Form Uq and Digital Twinning,” (under review), doi: https://doi.org/10.2139/ssrn.4960520.

[15] E. Reynders and G. De Roeck, “Reference-based combined deterministic–stochastic subspace identification for experimental and operational modal analysis,” *Mechanical Systems and Signal Processing*, vol. 22, pp. 617-637, Apr. 2008, doi: https://doi.org/10.1016/j.ymssp.2007.09.004.

[16] C. Soize and C. Farhat, “A nonparametric probabilistic approach for quantifying uncertainties in low-dimensional and high-dimensional nonlinear models,” *International Journal for Numerical Methods in Engineering*, vol. 109, no. 6, pp. 837–888, Jun. 2016, doi: https://doi.org/10.1002/nme.5312.

[17] R. Nayek, S. Chakraborty, and S. Narasimhan, “A Gaussian process latent force model for joint input-state estimation in linear structural systems,” *Mechanical Systems and Signal Processing*, vol. 128, pp. 497–530, Aug. 2019, doi: https://doi.org/10.1016/j.ymssp.2019.03.048.

[18] “Data-Driven Sparse Sensor Placement for Reconstruction: Demonstrating the Benefits of Exploiting Known Patterns,” *IEEE Control Systems*, vol. 38, no. 3, pp. 63–86, Jun. 2018, doi: https://doi.org/10.1109/mcs.2018.2810460.